Fast-ion phase-space tomography with wave-particle interactions in the ion cyclotron frequency range as prior

Downloaded from: https://research.chalmers.se, 2026-11-15 14:47 UTC

Citation for the original published paper (version of record):
[Person c6798b6e-d852-4177-b45e-640a84fd1416 not found], [Person b1a3b2eb-2bd3-4ae7-93b7-8a1b9fdaf2ba not found], [Person 34c8ccf4-2a86-4c1c-b1a4-ff7a049a4b77 not found] et al (2025). Fast-ion phase-space tomography with wave-particle interactions in the ion cyclotron frequency range as prior. Nuclear Fusion, 65(5). http://dx.doi.org/10.1088/1741-4326/adc400

N.B. When citing this work, cite the original published paper.

research.chalmers.se offers the possibility of retrieving research publications produced at Chalmers University of Technology. It covers all kind of research output: articles, dissertations, conference papers, reports etc. since 2004. research.chalmers.se is administrated and maintained by Chalmers Library

(article starts on next page)

nuclear fusion
IAEA

PAPER • OPEN ACCESS

Fast-ion phase-space tomography with wave–particle interactions in the ion cyclotron frequency range as prior

To cite this article: M. Rud *et al* 2025 *Nucl. Fusion* **65** 056008

View the article online for updates and enhancements.

You may also like

- Overview of T and D–T results in JET with ITER-like wall
C.F. Maggi, D. Abate, N. Abid et al.
- Modeling study of synergistic effects between lower hybrid and electron cyclotron current drive on EAST
S.G. Baek, M.H. Li, W. Choi et al.
- Simulations of ELM-induced tungsten melt flow across misaligned plasma-facing components
L. Vignitchouk, S. Ratynskaia and The ASDEX Upgrade Team

ARE YOU STRUGGLING TO SOURCE MATERIALS?

FIND OUT HOW GOODFELLOW IS HELPING LEAD THE WAY IN MATERIALS RESEARCH

We are proud to support fusion research, supplying materials for groundbreaking advancements since 1946. These include the 2022 LLNL achievement at the National Ignition Facility (NIF). This historic experiment marked the first-ever controlled fusion ignition, producing more energy from the reaction than was used to initiate it.

Click here to find out more about this story.

goodfellow
ADVANCED MATERIALS

EXPLORE OUR FULL RANGE OF IN STOCK MATERIALS.
- LITHIUM
- TUNGSTEN
- PALLADIUM SILVER ALLOYS AND MUCH MORE

SCAN THE QR CODE HERE OR VISIT:
goodfellow.com/nuclearfusionjournal

This content was downloaded from IP address 129.16.31.235 on 11/04/2025 at 08:49

OPEN ACCESS
IOP Publishing | International Atomic Energy Agency
Nuclear Fusion
Nucl. Fusion **65** (2025) 056008 (14pp)
https://doi.org/10.1088/1741-4326/adc400

Fast-ion phase-space tomography with wave–particle interactions in the ion cyclotron frequency range as prior

M. Rud[1,*], L.G. Eriksson[2], J. Eriksson[3], P.C. Hansen[4], O. Hyvärinen[5], H. Järleblad[4], Ye.O. Kazakov[6], S.B. Korsholm[1], M. Nocente[7], J. Rasmussen[1], B.C.G. Reman[6], A. Snicker[8], A. Valentini[1], Y. Dong[4], D. Moseev[9] and M. Salewski[1]

[1] Department of Physics, Technical University of Denmark, 2800 Kgs. Lyngby, Denmark
[2] Department of Space, Earth and Environment, Chalmers University of Technology, Gothenburg SE-412 96, Sweden
[3] Department of Physics and Astronomy, Uppsala University, 751 20 Uppsala, Sweden
[4] Department of Applied Mathematics and Computer Science, Technical University of Denmark, 2800 Kgs. Lyngby, Denmark
[5] Department of Mathematics and Statistics, University of Helsinki, Helsinki FI-00014, Finland
[6] Laboratory for Plasma Physics, LPP-ERM/KMS, 1000 Brussels, Belgium
[7] Department of Physics, University of Milano-Bicocca, 20126 Milano, Italy
[8] VTT, Technical Research Centre of Finland, Espoo, Finland
[9] Max-Planck-Institut für Plasmaphysik, Wendelsteinstr. 1, Greifswald 17491, Germany

E-mail: mrula@dtu.dk

Received 25 October 2024, revised 15 March 2025
Accepted for publication 21 March 2025
Published 2 April 2025

Abstract

The fast-ion distribution function in fusion plasmas can be inferred by inverting Doppler-shifted measurements from fast-ion diagnostics. The full fast-ion distribution function can be parametrised by three constants of motion with the addition of a binary index. However, with a limited number of measurements, cogent prior information must be added to regularise the inverse problem, enabling the reconstruction of the distribution function. In this paper, we demonstrate how to incorporate wave–particle interactions in the ion cyclotron range of frequencies (ICRFs) as prior information with the future ITER tokamak as a test case. We find that the addition of ICRF physics as prior information improves the reconstruction of a test ICRF-heated fast-ion distribution function in ITER using synthetic data based on the planned collective Thomson scattering sightlines and the planned gamma-ray spectroscopy sightlines.

* Author to whom any correspondence should be addressed.

Original Content from this work may be used under the terms of the Creative Commons Attribution 4.0 licence. Any further distribution of this work must maintain attribution to the author(s) and the title of the work, journal citation and DOI.

 © 2025 The Author(s). Published by IOP Publishing Ltd on behalf of the IAEA

The addition of such prior information is beneficial in the case of a limited phase-space coverage of fast-ion diagnostics.

Keywords: fast ions, prior information, tomography, wave–particle interactions

(Some figures may appear in colour only in the online journal)

1. Introduction

The study of energetic particles, or fast ions, in magnetic confinement fusion is of paramount importance due to their bimodal influence on the plasma state. On the one hand, they are beneficial as they are needed to sustain the high temperatures of the plasma for steady-state operation of fusion power plants, and they can suppress turbulence to improve the confinement of the plasma [1]. On the other hand, they can drive instabilities in the plasma, which can lead to fast-ion losses, damaging plasma-facing components and deteriorating the confinement of the plasma [2–13]. To optimise plasmas and mitigate such risks, it is advantageous to measure the fast-ion distribution function. However, it is not possible to measure it directly. It must be inferred by solving an ill-posed inverse problem [14]. To render the problem well-posed, one must regularise the inverse problem. A zoo of different types of regularisation exists which all ensure that the solution changes stably with the initial conditions. However, the choice of regularisation can greatly influence the reconstruction of the distribution function. It is therefore desirable to regularise the problem by incorporating prior information in the form of known physics, such that solutions, which do not satisfy the known physics, will be discarded. As we will see, this can be implemented in the framework of Tikhonov regularisation.

Velocity-space tomography [15–17] has been used to reconstruct fast-ion distribution functions in plasmas heated by neutral beam injection (NBI) [17–24] and by electromagnetic waves in the ion cyclotron range of frequencies (ICRFs) [25–27]. Several types of prior information have been demonstrated to improve the inference, e.g. non-negativity [28], the known location of NBI peaks [23, 28], numerical simulation [28], null-measurement velocity space [21, 28], monotonicity [22], collisional physics [23], near-isotropy [29], or anisotropy [30]. How to incorporate such prior information in the context of phase-space tomography has been described in [31–33]. This paper introduces a new type of prior information beneficial to phase-space tomography of energetic particles in magnetic confinement fusion, which is that of wave–particle interactions in the ion cyclotron range of frequencies (ICRF). Interactions between fast ions and waves of lower frequency, such as neoclassical tearing modes and certain Alfvén eigenmodes, have been studied extensively [13, 34–40] and constitute a natural extension beyond the scope of this work.

We are interested in determining regions of phase space where the fast-ion distribution function f is expected to have weak gradients. To this end we start by examining the orbit-averaged Fokker-Planck equation that governs the evolution of the distribution function of the resonating ions on time scales much longer than the orbit bounce time,

$$\frac{\mathrm{d}f}{\mathrm{d}t} = \langle C(f)\rangle + \langle Q(f)\rangle. \tag{1}$$

The orbit-averaged distribution function is a function of three invariants of the unperturbed particle motion, e.g. $f = f(E,\Lambda,P_\phi;\sigma)$ [41], where σ is a binary index needed to distinguish certain co-passing orbits from counter-passing orbits. The co-direction is defined to be in the direction of the plasma current which, in the case of ITER, is also in the direction of the toroidal magnetic field. E is the kinetic energy of the ion, $\Lambda = \mu B_0/E$ is the normalised magnetic moment, P_ϕ is the toroidal canonical angular momentum, $\langle C\rangle$ is the collision operator and $\langle Q\rangle$ is a quasi-linear operator describing the wave–particle interaction [41–43]. The collision operator has three components being collisional slowing down, energy diffusion and pitch angle scattering. At high energies, which is the region of interest here, the slowing-down term, i.e. collisions with electrons, dominates. In particular, the characteristic energy at which pitch-angle scattering becomes weak is given by a critical energy E_{crit} (see e.g. [44] for a convenient expression), and we consider energies $E \gg E_{\mathrm{crit}}$. The quasi-linear operator is of diffusion type in invariant space, and it is therefore expected that, when pitch-angle scattering is weak, the regions of low gradients in phase space should align well with the characteristics of this operator. This is the approach we examine here to find appropriate priors to the regularisation process.

In this paper, we will describe and demonstrate how to incorporate wave–particle interaction physics in the ion cyclotron range of frequencies as prior information into the inverse problems of phase-space tomography. With a limited number of fast-ion diagnostics available in ITER and other future tokamaks, any additional physics-based prior information is valuable when aiming to reconstruct a full fast-ion distribution function. In this paper, we consider the collective Thomson scattering (CTS) diagnostic [45–50] and the gamma-ray spectroscopy (GRS) diagnostic [51].

We consider an on-axis resonance scheme for heating deuterium, as well as an off-axis resonance heating scheme, typical for the three-ion heating scheme, where fast ions from the NBI constitute one of the species [52, 53]. These different heating schemes have been shown by velocity-space tomography to lead to qualitatively different phase-space distributions of MeV-range fast ions in the core of the plasma [25, 27], being symmetric in pitch, and asymmetric in pitch, respectively, which motivates the need for the tomography to accurately account for the ICRF heating scenario. The toroidal mode

number spectrum is dependent on the ICRF antenna phasing. We will describe how to include ICRF physics as prior information in the case of a single dominant mode number, as in the case of toroidally asymmetric ICRF waves with $\pm 90°$ phasing [54], as well as in the case of a symmetric mode number spectrum [55], as in the case of dipole phasing. Toroidally asymmetric ICRF waves have been shown to generate both a peaked radial pressure profile and a tail of energetic ions able to excite Alfvén eigenmodes depending on which phasing is chosen [56, 57].

The fast-ion phase space considered in this paper will be constants-of-motion phase space parameterised by (E, Λ, P_ϕ), as the wave–particle interactions in the ion cyclotron range of frequencies alter the constants of motion in known, predictable ways, which allows us to use it as prior information. These phase-space parameters are not the only ones with which one can perform orbit tomography. In [31], orbit tomography was performed in a pure 3D phase-space (E, p_m, R_m) (not requiring an extra binary parameter σ), where R_m is the maximum major radius coordinate of the fast-ion orbit, and p_m is the pitch at the maximum major radius coordinate [58–61]. However, the ICRF physics are more conveniently formulated in constants-of-motion phase space.

The rest of the paper is organised as follows. In section 2 we review the characteristics of ion motion in constants-of-motion phase space, and in velocity space, for ICRF heating. How to incorporate wave–particle interactions, and in particular ICRF heating, as prior information in the inverse problem is explained in section 3. The new regularisation technique is also demonstrated on a test distribution in the $\sigma = 1$ part of phase space, which acts as a simple model of an ICRF-tail distribution. Section 4 concludes the paper.

2. Characteristics of ion motion in phase space for ICRF heating

It is of interest to understand the energetic particle distribution function due to ICRF heating, which generates a tail towards high energies. For the ICRF heating wave to resonate with an ion at a specific location in position space, the following local resonance condition must be satisfied [41],

$$\omega = n\omega_{ci} + k_\parallel v_\parallel, \tag{2}$$

where ω is the angular frequency of the heating wave, n is the cyclotron harmonic of the wave, ω_{ci} is the local ion cyclotron frequency, $k_\parallel$ is the parallel wave number and $v_\parallel$ is the parallel velocity of the ion. Here, $k_\parallel v_\parallel$ reflects the Doppler shift of particles due to motion along the magnetic field direction. When the electromagnetic wave interacts with the fast ions, it exchanges energy as well as canonical toroidal angular momentum P_ϕ and normalised magnetic moment Λ. These are given by

$$E = \frac{1}{2} m \left(v_\parallel^2 + v_\perp^2 \right), \tag{3}$$

$$\Lambda = \frac{\mu B_0}{E} = \frac{m v_\perp^2}{2B} \frac{B_0}{E}, \tag{4}$$

$$P_\phi = mR \frac{B_\phi}{B} v_\parallel + q\Psi_p, \tag{5}$$

where m is the mass of the fast ion, R is the major radial coordinate, $v_\perp$ is the fast-ion velocity perpendicular to the magnetic field, q is the electrical charge of the particle, B is the magnetic field strength, B_0 is the magnetic field strength on the magnetic axis, B_ϕ is the toroidal component of the magnetic field, μ is the magnetic moment and Ψ_p is the poloidal magnetic flux per radian. For fast ions interacting with the wave according to the resonance condition in equation (2), the changes in energy, canonical toroidal angular momentum and normalised magnetic moment are related by [41, 43, 62]

$$\Delta P_\phi = \frac{N}{\omega} \Delta E, \tag{6}$$

$$\Delta \Lambda = (\Lambda_\infty - \Lambda) \frac{\Delta E}{E}, \tag{7}$$

where $\Lambda_\infty = n\omega_{c0}/\omega$, N is the toroidal mode number of the wave and ω_{c0} is the cyclotron frequency on the magnetic axis. For wave frequencies much lower than the cyclotron frequency, such as Alfvén waves, the conservation of magnetic moment replaces equation (7), and the characteristics of the phase-space flow are given by the intersections of the surfaces in phase space given by equation (6) and $\Delta\mu = 0$, respectively [63]. From equation (6), we see that high-frequency waves primarily cause energy transport, whereas low-frequency waves primarily cause spatial transport (given by ΔP_ϕ).

Equations (6) and (7) suggest that a particle accelerated by an ICRF wave will move along the characteristic phase-space direction described by the vector $\epsilon = (\Delta\Lambda, \Delta P_\phi, \Delta E)^{\mathrm{T}}$, with the normalised unit vector defined by

$$\hat{\epsilon} = \frac{1}{\|\epsilon\|} \begin{pmatrix} \Delta\Lambda \\ \Delta P_\phi \\ \Delta E \end{pmatrix} = \frac{1}{\|\epsilon\|} \begin{pmatrix} (\Lambda_\infty - \Lambda)/E \\ N/\omega \\ 1 \end{pmatrix} \Delta E, \tag{8}$$

where the hat-notation denotes that this is a unit vector, and where $\|\cdot\|$ is the two-norm. One such unit vector exists for every point in phase space. A streamline is defined as a curve tangent to this unit vector in every point. Particles heated by ICRF heating will hence follow these streamlines. Since a continuous stream of particles flows along the streamlines, any gradients in the distribution function along the streamlines are expected to be small. We therefore incorporate the physics of ICRF heating by penalising large gradients along the streamlines.

Both on-axis resonance heating and off-axis resonance heating can be treated by varying Λ_∞ as the only parameter. On-axis resonance is defined by $\Lambda_\infty = 1$, whereas off-axis resonance is defined by $\Lambda_\infty \neq 1$ leading to qualitatively different streamlines. As noted in the introduction, the off-axis resonance is typical for the three-ion heating scheme, when the NBI ions are used as the absorbing species, as they then satisfy the resonance condition in the plasma centre due to their Doppler shift. In the following we will treat both cases and show examples of streamlines calculated from parameters typical of expected ITER scenarios.

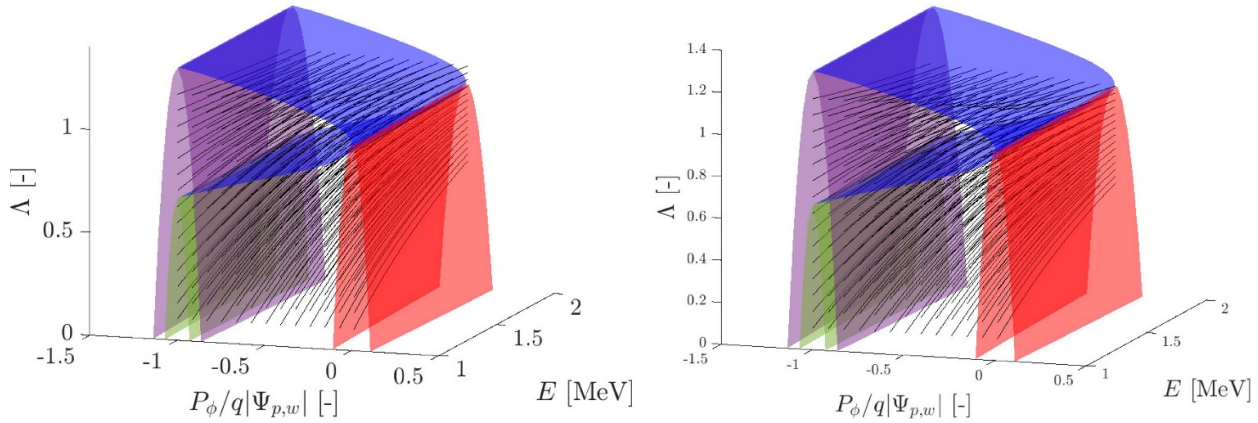

(a) On-axis resonance heating (b) Off-axis resonance heating

Figure 1. Phase-space streamlines shown in black for the interaction between fast-ion orbits and an ICRF wave in the ITER baseline plasma scenario. Topological boundaries have been assigned different colours to distinguish them more easily. (*a*) On-axis resonance heating case with $n = 1$, $N = -30$ and $\omega = n\omega_{c0}$. (*b*) Off-axis resonance heating case with $n = 1$, $N = -30$ and $\omega = n\omega_{c0}/0.85$.

Taking on-axis resonance ICRF heating as an example in a typical ITER plasma, we set $N = -30$, $n = 1$ and $\omega = n\omega_{c0}$, and use the equilibrium with IMAS-id: #130501-1 [64, 65] with magnetic field on axis $B_0 = 5.3$ T, and a NBI energy of 1 MeV. The resulting streamlines in phase space are illustrated in figure 1(*a*). This figure illustrates the directions associated with each point in (E, Λ, P_ϕ) space as given by equation (8), leading to a pattern of streamlines in analogy to streamlines in fluid mechanics. Examples of such streamlines are also plotted in [62]. We note that the phase-space streamlines are identical for all harmonics n when the injected wave frequency ω is given by $\omega = n\omega_{c0}$. As an example of off-axis resonance heating, we also consider $N = -30$, $n = 1$ and $\omega = n\omega_{c0}/0.85$. The streamlines in phase for the off-axis resonance are illustrated in figure 1(*b*). We will consider these two ICRF heating schemes throughout the paper, where in one case $\omega = n\omega_{ci}$ on the magnetic axis, and in the other case $\omega = n\omega_{ci}$ off axis. The coloured surfaces in figure 1 denote topological boundaries between different orbit types [66]. As ICRF heating draws particles along these streamlines, it leads to the formation of high energy tails in the phase-space distribution function. Notice that the streamlines primarily go along the E-direction, and to a lesser extent in the Λ-direction, with the change in P_ϕ being negligible for these frequencies. Figures 1(*a*) and (*b*) look similar, but the streamlines approach different Λ values as the energy increases. Specifically $\Lambda_\infty = 1$ for the on-axis resonance heating ICRF scheme and $\Lambda_\infty = 0.85$ for the off-axis resonance heating scheme.

Assuming the NBI ions resonate with an electromagnetic wave, the parametric curves of the streamlines are found by taking small steps dE and dΛ and integrating both sides of equation (7) after separating the variables,

$$\int_{E_0}^{E} \frac{\mathrm{d}E'}{E'} = \int_{\Lambda_0}^{\Lambda} \frac{\mathrm{d}\Lambda'}{(\Lambda_\infty - \Lambda')}, \tag{9}$$

such that

$$E = E_0 \frac{\Lambda_\infty - \Lambda_0}{\Lambda_\infty - \Lambda}. \tag{10}$$

As the streamlines in (E, Λ, P_ϕ) space are perhaps rather abstract, we will relate them to the $(v_\parallel, v_\perp)$ space commonly used to illustrate distribution functions typical for ICRF heating [67, 68]. The 3D streamlines in constants-of-motion space suggest 2D streamlines in velocity space in any given point (R, z). The streamlines in (E, p)-space are found by expressing Λ in terms of the pitch $p = v_\parallel/v$, see equation (4),

$$\Lambda = \left(1 - p^2\right) B_0 / B\left(R, z\right). \tag{11}$$

From equation (10), we then get [53]

$$p\left(E\right)^2 = \frac{E_0}{E} p_0^2 + p_\infty^2 \left(1 - \frac{E_0}{E}\right), \tag{12}$$

where p_0 and p_∞ are obtained from (11),

$$p_0^2 = 1 - \frac{B\left(R, z\right)}{B_0} \Lambda_0, \; p_\infty^2 = 1 - \frac{B\left(R, z\right)}{B_0} \Lambda_\infty. \tag{13}$$

In velocity space, this becomes

$$v_\perp^2 = \frac{1 - p_\infty^2}{p_\infty^2} v_\parallel^2 - \frac{p_0^2 - p_\infty^2}{p_\infty^2} v_0^2. \tag{14}$$

In figure 2, the streamlines in velocity space are shown at the magnetic axis as well as at three different radial locations along the midplane. The top row represents the on-axis resonance heating case, and the bottom row represents the off-axis resonance heating case. In the on-axis resonance case we have $\Lambda_\infty = 1$, such that the asymptotic resonance is a vertical line at $R = R_0$, as shown by the green lines in figure 2, which reflects that the on-axis resonance ICRF heating gives kicks in the $v_\perp$ direction. The tilt of the asymptotic resonance line for $R = R_0$ in figure 2(*e*) is due to the off-axis resonance $\Lambda_\infty \neq 1$. When the same ion phase-space flow along streamlines due to ICRF heating is observed at different locations in

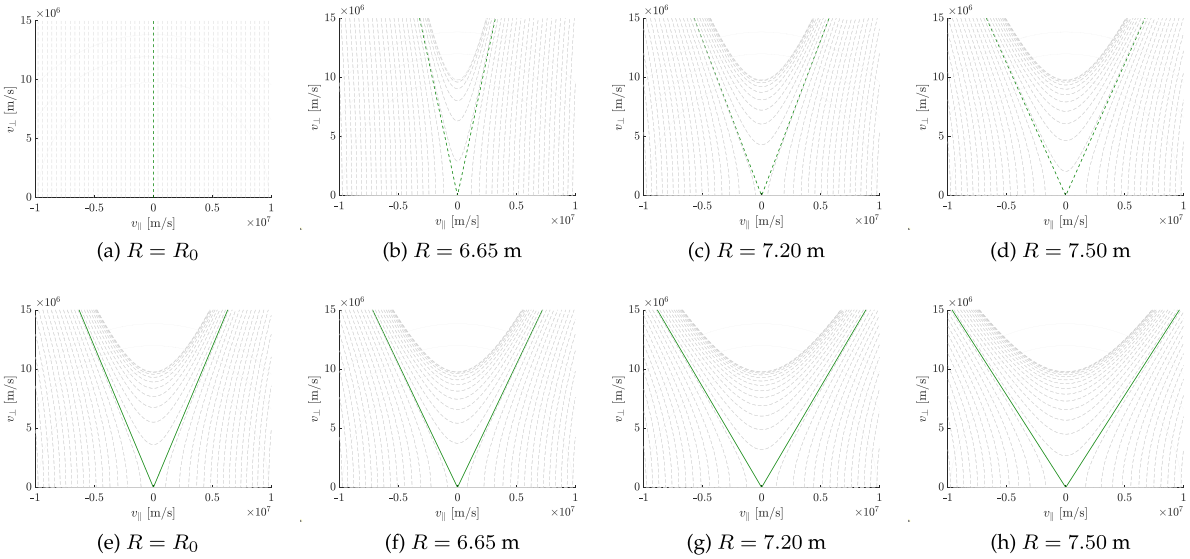

(a) $R = R_0$ (b) $R = 6.65$ m (c) $R = 7.20$ m (d) $R = 7.50$ m

(e) $R = R_0$ (f) $R = 6.65$ m (g) $R = 7.20$ m (h) $R = 7.50$ m

Figure 2. Velocity-space streamlines corresponding to the cases in figure 5 with matching colours for on-axis resonance heating in (*a*)–(*d*), and off-axis resonance heating in (*e*)–(*h*). The dashed (solid) green lines are the asymptotic resonances in the on-axis (off-axis) resonance case. Streamlines throughout velocity space are shown for reference in grey dashed lines. The faint solid-line semicircles are contours of constant energy, of 1 MeV, 1.5 MeV and 2 MeV, respectively. The streamlines on the magnetic axis are shown in (*a*) and (*e*) for visualisation purposes.

(R, z), the conservation of magnetic moment results in a part of the energy being converted from $v_\perp$ to $v_\parallel$, such that the asymptotic resonance line, shown in green in figure 2, has a tilt in velocity-space, which increases with the distance from the magnetic axis, where the ions are heated. The asymptotic resonance line in velocity space for each spatial location in (R, z) is found from (11),

$$v_{\perp,\infty}^2 = \frac{\Lambda_\infty}{B_0/B\,(R,z) - \Lambda_\infty} v_{\parallel,\infty}^2. \tag{15}$$

The asymptotic resonance lines for negative and positive $v_\parallel$ result from counter-passing and co-passing orbits resonating with the wave, respectively. As the streamlines in 3D phase space are used as prior information in this study, the streamlines in 2D velocity space can likewise be used as prior information in velocity-space tomography.

3. The inverse problem

The fast-ion distribution function cannot be measured directly, but must be inferred from diagnostic measurements, which can be based on nuclear reactions resulting in neutrons leaving the plasma, or charge-exchange reactions emitting photons, both of which can be observed by fast-ion diagnostic instruments. The diagnostic signal often depends linearly on the fast-ion distribution function given by a Fredholm equation of the first kind [58–60, 69, 70]

$$s\,(u_1, u_2, \varphi) = \sum_{\sigma=\pm 1} \iiint \left(w_{\mathrm{COM}}^{(3D)}\,(u_1, u_2, \varphi, E, \Lambda, P_\phi; \sigma) \times f_{\mathrm{COM}}^{(3D)}\,(E, \Lambda, P_\phi; \sigma) \right) \mathrm{d}P_\phi \mathrm{d}\Lambda \mathrm{d}E, \tag{16}$$

where $f_{\mathrm{COM}}^{(3D)}$ is the fast-ion distribution function in constant-of-motion phase space, and $w_{\mathrm{COM}}^{(3D)}$ is a weight function quantifying the diagnostic sensitivity in phase space. Here a generic diagnostic is considered as in [33, 71], assumed to measure u, the fast-ion velocity projected onto the line of sight of the diagnostic, as this quantity may lead to a Doppler shift of the signal, which is the fundamental property used to infer which fast-ion orbit is likely to have been observed. This is common for many different fast-ion diagnostics, such as FIDA spectroscopy [72–76], CTS [77], GRS [78, 79] and neutron emission spectroscopy [25]. The finite resolution of a diagnostic instrument is denoted by the edges of each measurement bin u_1 and u_2, and φ is the viewing angle between the line of sight and the magnetic field vector in the measurement volume. The viewing angle has a paramount influence on to which extent the observed signal will be Doppler-shifted. Discretising this linear equation, we get the matrix–vector equation

$$\mathbf{s} = W\mathbf{f}, \tag{17}$$

where $\mathbf{s}$ is a vector containing the measurements, $\mathbf{f}$ is the vectorised fast-ion distribution function and W is the weight matrix, where each row is a weight function. In this study, we consider the three GRS lines of sight [51], and the seven CTS measurement volumes [48] planned for ITER, whose weight functions have been calculated using the procedure described in [71]. We thus have 10 spectra, which all have viewing angles close to $\varphi \approx 90°$.

The weight matrix is ill-conditioned, such that a regular least squares inversion produces nonsensical results. The inverse problem of calculating $\mathbf{f}$ from $\mathbf{s}$ and W is ill-posed and the ill-conditioned weight matrix tends to amplify noise in $\mathbf{s}$ in the reconstruction of $\mathbf{f}$. Therefore regularisation of the

inverse problem is needed. A widespread technique adopted is Tikhonov regularisation [80]. The general-form Tikhonov regularisation is formulated as

$$\bar{f}_\lambda = \min_{\mathbf{f}} \left(\|\mathbf{s} - W\mathbf{f}\|_2^2 + \lambda^2 \|L\mathbf{f}\|_2^2 \right), \tag{18}$$

where L is the regularisation matrix of choice, which determines which property of $\mathbf{f}$ is minimised in the reconstruction. The regularisation parameter λ controls to which extent the reconstruction should fit the observed data relative to the regularisation term. The addition of the regularisation term in the least-squares minimisation forces the inversion to change stably with the noisy signal $\mathbf{s}$. However, it also means that we cannot achieve a perfect reconstruction, even with completely noise-free measurements.

Choosing $L = \mathbb{1}$ to be the identity matrix is referred to as zeroth-order Tikhonov regularisation, which penalises large values in $\mathbf{f}$. Choosing L to be a discrete approximation of the gradient operator ∇ penalises large gradients in $\mathbf{f}$ and thus promotes smooth solutions. This is referred to as first-order Tikhonov regularisation. Smooth solutions are also promoted by collision physics, which tends to smooth out the distribution function. By choosing $L = L_1 \approx \nabla$, collision physics can be incorporated into the problem as prior information. This was studied in more detail in the context of phase-space tomography in [33]. We will use the ICRF physics encoded in equations (6) and (7) as prior information in a standard Tikhonov regularisation framework. To penalise gradients along the phase-space streamlines suggested by equations (6) and (7) more than across them, we need to formulate the projection matrix onto the characteristics in each point in phase space, which is

$$\begin{aligned}\hat{\epsilon}_m \hat{\epsilon}_m^T &= \frac{1}{\|\epsilon_m\|^2} \begin{pmatrix} D_{\Lambda_m\Lambda_m} & D_{\Lambda_m P_\phi} & D_{\Lambda_m E} \\ D_{P_\phi\Lambda_m} & D_{P_\phi P_\phi} & D_{P_\phi E} \\ D_{E\Lambda_m} & D_{EP_\phi} & D_{EE} \end{pmatrix} \\ &= \frac{1}{\|\epsilon_m\|^2} \begin{pmatrix} \frac{(\Lambda_\infty - \Lambda_m)^2}{E_m^2} & \frac{N}{\omega}\frac{\Lambda_\infty - \Lambda_m}{E_m} & \frac{\Lambda_\infty - \Lambda_m}{E_m} \\ \frac{N}{\omega}\frac{\Lambda_\infty - \Lambda_m}{E_m} & \frac{N^2}{\omega^2} & \frac{N}{\omega} \\ \frac{\Lambda_\infty - \Lambda_m}{E_m} & \frac{N}{\omega} & 1 \end{pmatrix}, \end{aligned} \tag{19}$$

where we have omitted the overall factor of $(\Delta E)^2$, as it can be absorbed in the normalisation. The index $m = 1, \ldots, M = M_E M_\Lambda M_{P_\phi}$ runs over all of phase space with M_i being the number of grid points in the i'th dimension, and the elements D_{ij} are the ICRF diffusion tensor elements [41, 43].

In the case of ICRF dipole phasing, where the spectrum of toroidal mode numbers N is symmetric around zero, such that the kicks in the P_ϕ direction partially cancel out, the off-diagonal terms in equation (19) that are linear in N are discarded. In fact, as we see in figure 1, the characteristic changes in P_ϕ are small for these high-frequency waves even for a finite mode number. Furthermore, since we are only interested in approximately determining the directions in which the gradients of the distribution function are weak, we can discard the terms linear in N for both asymmetric and symmetric mode number spectra. For completeness, we keep the terms when writing out the regularisation matrix explicitly. The modified first-order Tikhonov regularisation matrix, when penalising according to the wave–particle interaction characteristics, then becomes [33]

$$\begin{aligned}\hat{L}_1^{(\mathrm{ICRF})} &= K^{(M,3)} \left(\bigoplus_{m=1}^{M} \hat{\epsilon}_m \hat{\epsilon}_m^T \right) K^{(3,M)} L_1 \\ &= \begin{pmatrix} \mathbf{D}_{\Lambda\Lambda}(\mathbf{\Lambda},\mathbf{E}) & \mathbf{D}_{\Lambda P_\phi}(\mathbf{\Lambda},\mathbf{E}) & \mathbf{D}_{\Lambda E}(\mathbf{\Lambda},\mathbf{E}) \\ \mathbf{D}_{P_\phi\Lambda}(\mathbf{\Lambda},\mathbf{E}) & \frac{N^2}{\omega^2}\mathbb{1}_M & \frac{N}{\omega}\mathbb{1}_M \\ \mathbf{D}_{E\Lambda}(\mathbf{\Lambda},\mathbf{E}) & \frac{N}{\omega}\mathbb{1}_M & \mathbb{1}_M \end{pmatrix} L_1, \end{aligned} \tag{20}$$

where $\mathbf{D}_{ij}(\mathbf{\Lambda},\mathbf{E})$ are $M \times M$ diagonal matrices with $D_{ij}(\Lambda_m, E_m)/\|\epsilon_m\|^2$ from equation (19) on the main diagonals, with the (i,j) indices running over (Λ, P_ϕ, E), and where $\mathbf{\Lambda} = (\Lambda_1, \ldots, \Lambda_m, \ldots, \Lambda_M)^{\mathrm{T}}$ is a vector with the Λ-value in all points in phase space, and likewise for $\mathbf{E}$. $\mathbb{1}_M$ is the $M \times M$ identity matrix. The sign $\bigoplus$ represents a direct matrix sum, and $K^{(v,w)}$ is the commutation matrix. We note that the three-by-three matrix above is exactly the one defined by equations (11)–(16) of [41] up to a constant factor of ω^2. This regularisation matrix $\hat{L}_1^{(\mathrm{ICRF})}$ is proposed to be suitable for reconstructing ICRF-tails of fast-ion distribution functions. We will demonstrate this in the next section. When adding ICRF heating as prior information, the total regularisation matrix used can be expressed as

$$L = \begin{pmatrix} \hat{L}_1^{(\mathrm{ICRF})} \\ L_1 \end{pmatrix}, \tag{21}$$

where the upper row reflects smoothness along the ICRF characteristics and the lower row reflects smoothness of $\mathbf{f}$ in any direction due to collisions, here effected by standard first-order Tikhonov regularisation. Note that we need some regularisation everywhere in phase space in order to have a well-behaved inverse problem. In order to promote the ICRF regularisation we keep the corresponding regularisation parameter a factor 10 larger than the first-order Tikhonov regularisation parameter.

The ICRF regularisation is only implemented in those phase-space coordinates where the resonance condition is satisfied. The constants-of-motion phase space is parametrised by (3)–(5). The resonance condition is (2), and we make the assumption [62, 81],

$$k_\parallel \approx k_\phi = \frac{N}{R}. \tag{22}$$

Substituting $v_\parallel$ in (5) using the resonance condition and using (22), we get

$$P_{\phi,\mathrm{res}} = \left(\omega - n\frac{qB}{m} \right) \frac{mR^2 B_\phi}{NB} + q\Psi_p. \tag{23}$$

Knowing the magnetic equilibrium in (R,z), we can find the value $P_{\phi,\mathrm{res}}$ that satisfies the resonance condition in all spatial (R,z) coordinates. The distribution function will be drawn

along the streamlines in phase space to some degree, depending on how much the ion interacts with the wave. Therefore, it is justified that we penalise the gradient along the streamlines in the region of phase space given by equation (23).

We will illustrate where the resonance condition is satisfied, i.e. where we apply our ICRF regularisation, using the ITER test cases. The ICRF system for ITER consists of two antenna arrays injecting waves in the 40–55 MHz frequency range [82]. In this test problem we consider the parameters of the electromagnetic wave to be $\omega/2\pi = 41$ MHz, the cyclotron harmonic is either $n = 1$ or $n = 2$, and the toroidal mode number is chosen to be $N = -30$ in the on-axis resonance heating case. The second harmonic heating case can be achieved in reduced field scenarios. For the off-axis resonance heating, we have $\omega/2\pi = 48$ MHz, $n = 1$ and $N = -30$. The P_ϕ values satisfying the resonance condition in all (R, z) points are shown in the left column of figure 3 for different heating scenarios. Since E, Λ and P_ϕ are not independent if the spatial location is fixed, we can solve for Λ in all (R, z) points for each energy,

$$\Lambda_{\text{res}} = \left(\frac{E_{\text{res}}}{B} - \frac{(P_{\phi,\text{res}} - q\Psi)^2 B}{2mR^2 B_\phi^2} \right) \frac{B_0}{E_{\text{res}}}. \tag{24}$$

In the right column of figure 3, Λ_{res} is shown for $E_{\text{res}} = 1$ MeV. Since Λ must be positive, we can immediately discard all solutions of equation (24) which are negative. These negative values for Lambda are shown as the white regions in the right column in figure 3, but 1 MeV particles in the white regions can move along their orbits to reach the region where resonance is possible. However, deeply trapped orbits that never leave the white region will never resonate with the ICRF wave, and hence the ICRF regularisation will not be applied in this region of (E, Λ, P_ϕ) space as we will show in the following. It is noted that by solving the resonance condition (2) for the triplets $(E_{\text{res}}, \Lambda_{\text{res}}, P_{\phi,\text{res}})$ we immediately get the familiar vertical resonance region in (R, z), as can e.g. be seen in [83]. Our approach also includes the broadening of the resonance region for increasing fast-ion energies, as provided by the Doppler shift. Here, we emphasise that we can incorporate any heating scheme by adjusting the parameters in equations (2), (6) and (7) accordingly.

Knowing which (E, Λ, P_ϕ) triplets that resonate in each (R, z) point, we can check whether these triplets constitute valid orbits. Doing this in all energy planes, we thus have a map $\mathcal{X}$ denoting whether or not each orbit can resonate with the ICRF heating wave somewhere in the plasma,

$$\mathcal{X}_{ijk} = \begin{cases} 1, \text{ if } (P_{\phi,i}, \Lambda_j, E_k) \text{ is a valid orbit-triplet,} \\ 0, \text{ if } (P_{\phi,i}, \Lambda_j, E_k) \text{ is not a valid orbit-triplet.} \end{cases} \tag{25}$$

In figure 4 the (R, z) coordinates where valid orbits are found to possibly resonate with the heating wave is shown for three different fast-ion energies for the $n = 1$ on-axis resonance heating scheme and the off-axis resonance heating scheme shown above. We observe a resonance region similar to the cold resonance layer, which broadens for higher energies due to the increasing fast-ion Doppler shifts. The corresponding maps in constants-of-motion phase space depend on the numerical resolution used in (R, z)-space, when evaluating equations (23) and (24). As the resolution in (R, z) goes to infinity, we find that all orbits traversing the resonance region in (R, z) satisfy the resonance condition somewhere. The ICRF regularisation will then be implemented on the phase-space coordinates satisfying the resonance condition, i.e. all coordinates except the deeply trapped orbits and some stagnation orbits, which never enter the resonance region in (R, z). We note that an ICRF heating scheme can have a barrier region in energy, where the wave–particle interaction becomes weak [83], which could be included as additional prior information by only regularising up to the barrier energy and penalising any phase-space densities for energies above the barrier energy. However, we have not included this additional prior information here.

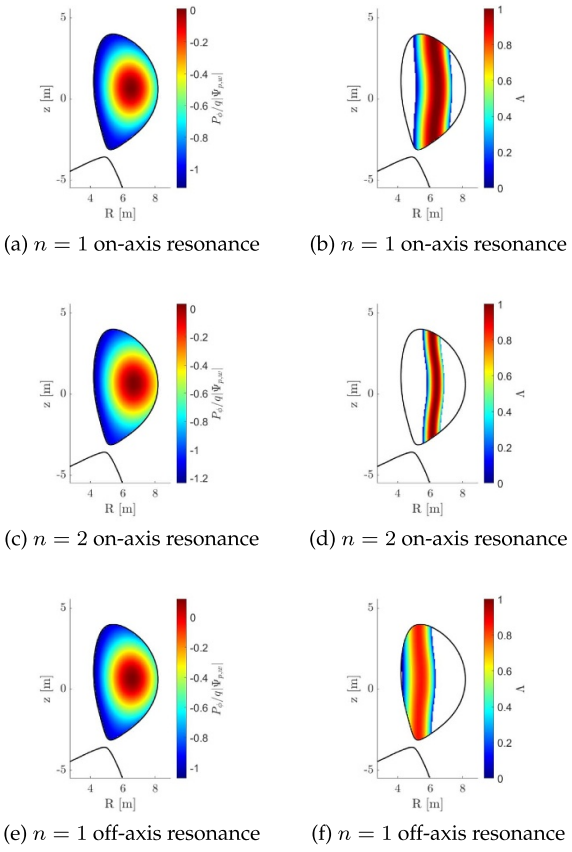

(a) $n = 1$ on-axis resonance (b) $n = 1$ on-axis resonance

(c) $n = 2$ on-axis resonance (d) $n = 2$ on-axis resonance

(e) $n = 1$ off-axis resonance (f) $n = 1$ off-axis resonance

Figure 3. Left column: values of P_ϕ satisfying the resonance condition everywhere in physical space. (*a*) On-axis resonance first-harmonic heating case. (*c*) On-axis resonance second-harmonic heating case. (*e*) Off-axis resonance heating case. Right column: values of Λ satisfying the resonance condition everywhere in physical space for a fast-ion energy $E = 1$ MeV. Only positive values of Λ_{res} are shown. (*b*) On-axis resonance first-harmonic heating case. (*d*) On-axis resonance second-harmonic heating case. (*f*) Off-axis resonance heating.

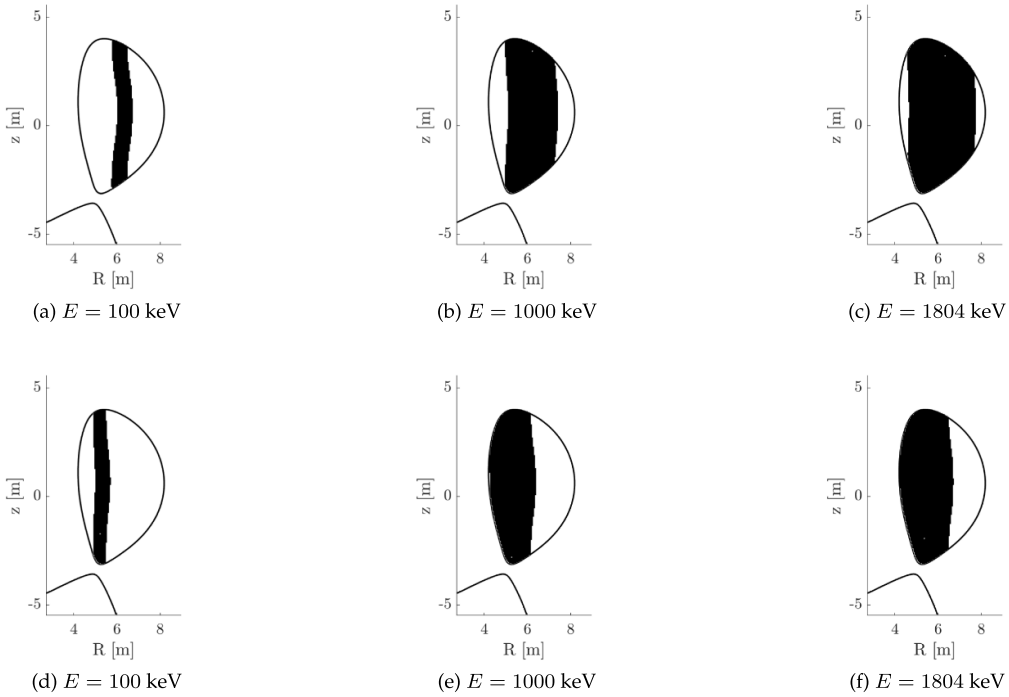

(a) $E = 100$ keV (b) $E = 1000$ keV (c) $E = 1804$ keV

(d) $E = 100$ keV (e) $E = 1000$ keV (f) $E = 1804$ keV

Figure 4. Resonance region in (R, z) for three different fast-ion energies. (a)–(c) On-axis resonance $n = 1$ heating case. (d)–(f) Off-axis resonance heating case. The size of the resonance region broadens with the fast-ion energy, as an increasing amount of Doppler shift is available.

3.1. True test distribution

To create a test fast-ion distribution in constants-of-motion phase space, we place a Gaussian blob in the $E = 1$ MeV energy plane, to mimic the injection energy of the neutral beam injectors in ITER. The left column of figure 5 shows the orbit topology in a plane of constant energy at the NBI injection energy 1 MeV in constants-of-motion phase space, see e.g. [66, 71]. The dashed line shows which orbits the NBI can inject for ionization along the beam path from the low-field side plasma edge to the plasma centre. We study three different NBI ion birth locations at $R = 6.65$ m, at $R = 7.20$ m, and at $R = 7.50$ m, respectively, all on the midplane, as in figure 2. In an energy slice in constant-of-motion space, each position in (R, z) corresponds to a position-space parabola, which is the locus of all orbits traversing that position, and is defined in [71], and the intersection between the NBI path and the position-space parabola gives possible (E, Λ, P_ϕ)-triplets of the injected ion. The right branch of the position-space parabola corresponds to co-going orbits and the left-branch corresponds to counter-going orbits [71, 84]. As the injection of particles is in the co-going direction, we only mark in figure 5 the crossing of the NBI path and the right branch of the position-space parabola.

All the orbits in the Gaussian blob satisfying the resonance condition are then transported upwards in energy in steps of 1 keV, and accordingly in P_ϕ and Λ according to equations (6) and (7). The streamlines in (Λ, E), given by equation (10), can be seen in the right column of figure 5. After each kick, the orbit gets an additional kick only if it still satisfies the resonance condition. In this way, we create test distributions, which will be considered to be the true distributions $\mathbf{f}_{\text{true}}$ in the inverse problems.

3.2. Reconstructions

In contrast to velocity-space tomography, phase-space tomography allows us to combine diagnostic information from different locations in the plasma. This will be utilised in this study by considering the CTS and GRS sightlines planned for ITER. To reconstruct the test distribution, we calculate 10 synthetic spectra based on the planned CTS and GRS diagnostics for ITER, and example spectra are shown in figure 6 for the test distribution shown in the upper row of figure 10. These spectra are calculated by inserting $\mathbf{f}_{\text{true}}$ in equation (17) and illustrate the measurement data vector $\mathbf{s}$ that we use for the inversion as a synthetic model for the measurement data we can expect to measure in ITER measurements. The CTS measurement volumes are modelled as Gaussian blobs with variances as given by table 4 in [48]. The GRS sightlines are modelled as Gaussian beams. The spectra are comprised of the projected velocity of fast ions, as described in the beginning of this section. Correspondingly, no instrumental response function is taken into account. The central part of each spectra is discarded, as this is dominated by thermal ions. The weight functions are resolved on a $27 \times 27 \times 27$ phase-space grid with 99 measurement bins in each spectrum, such that $W \in \mathbb{R}^{990 \times 19683}$. The Index label in figure 6 denotes the 990 rows of W. Before the inversion of the spectra, random noise is added $\mathbf{s} \to \mathbf{s} + \mathbf{e}$ with $\mathbf{e} \sim \mathcal{N}(0, C_\mathbf{s})$ drawn from a normal distribution with zero mean and a diagonal covariance matrix, given by

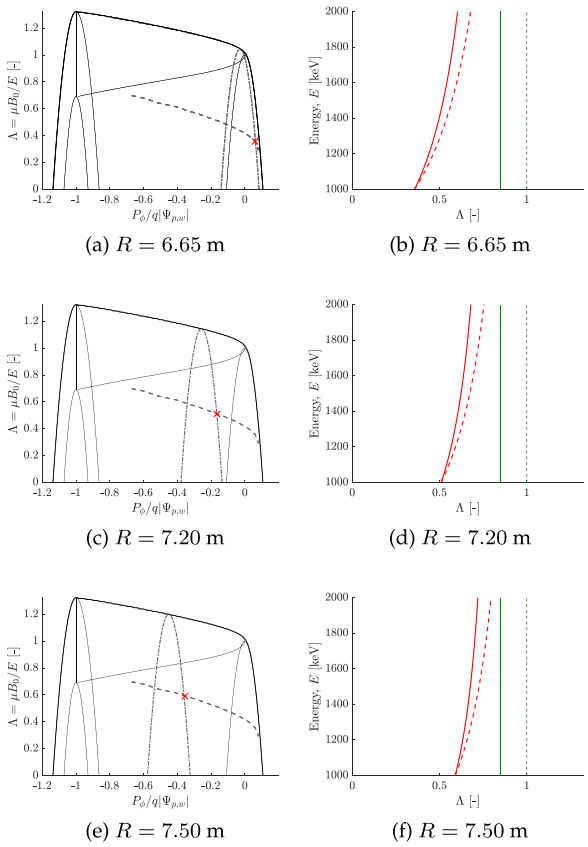

Figure 5. (*a*), (*c*) and (*e*): The dashed line traverses the orbits born along the centre of the NBI beamline on the low-field side. The dashed–dotted grey parabolas denote which orbits pass through three different radial locations on the midplane, which is noted in each subcaption. The coloured crosses denote co-passing fast-ion orbits born along the beam on the three different locations. (*b*), (*d*) and (*f*): Streamlines in phase space given by equation (10) for on-axis resonance heating (dashed line) and off-axis resonance heating (solid line). The green vertical lines are the asymptotic resonances $\Lambda_\infty = n\omega_{c0}/\omega$ in the on-axis resonance (dashed) and off-axis resonance (solid) cases, respectively.

$$(C_{\mathbf{s}})_{ij} = \begin{cases} \max\left\{0.02 s_i, 10^{-3}\max\{\mathbf{s}\}\right\}, & i = j, \\ 0, & i \neq j. \end{cases} \tag{26}$$

For the purposes of this study, we simply parametrise the noise for both diagnostics as given in equation (26), although in reality signal-independent noise terms would also contribute depending on the type of diagnostic considered. If the inverse and forward models are exactly the same, the inversion of synthetically generated data is unrealistically accurate, which is known as an 'inverse crime' in the inverse problem community. In order to use an inverse model different from the forward model, we interpolate the weight matrix onto a slightly coarser phase-space grid with a resolution of $25 \times 25 \times 25$, on which we calculate the inverse problem. To treat the CTS spectra and GRS spectra on an equal footing, we normalise the CTS spectra with 2% of the maximum of all measured CTS spectra, and we normalise the GRS spectra with 2% of the maximum of all measured GRS spectra. The finite-difference

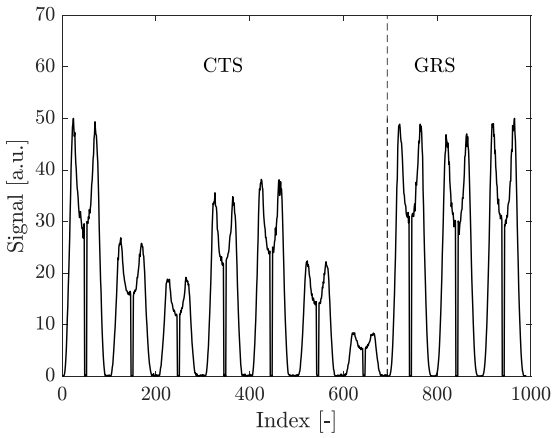

Figure 6. Synthetic spectra with noise. The spectra are normalised with the measurement uncertainty to treat CTS and GRS on an equal footing. The first seven spectra are based on the CTS diagnostic planned for ITER, and the last three spectra are based on the GRS diagnostic planned for ITER. All spectra are resolved across a range of projected velocity of $[-1.4, 1.4] \cdot 10^7$ m s^{-1}.

approximation of the gradient operator used in (20) penalises the pixel-wise difference along each axis in phase space. Since the axes have different units, we normalise each axis such that they are dimensionless, and the elements of $\boldsymbol{\epsilon}$ are normalised correspondingly. Λ and $\Delta\Lambda$ are already dimensionless, but in the definition of $\boldsymbol{\epsilon}$, equation (6) is replaced by

$$\Delta\tilde{P}_\phi = \frac{N}{\tilde{\omega}}\Delta\tilde{E}, \tag{27}$$

where

$$\tilde{P}_\phi = \frac{P_\phi}{q|\Psi_{\mathrm{p,w}}|}, \quad \tilde{E} = \frac{E}{E_{\mathrm{NBI}}}, \quad \tilde{\omega} = \omega\frac{q|\Psi_{\mathrm{p,w}}|}{E_{\mathrm{NBI}}}, \tag{28}$$

where $E_{\mathrm{NBI}} = 1$ MeV is the NBI injection energy, and $\Psi_{\mathrm{p,w}}$ is the poloidal magnetic flux per radian at the last closed flux surface. To quantify how well the true distribution function is reconstructed, we calculate the two-norm of the difference between the true distribution function and the reconstruction as a relative error norm,

$$\varepsilon = \frac{\|\bar{\mathbf{f}}_\lambda - \mathbf{f}_{\mathrm{true}}\|_2}{\|\mathbf{f}_{\mathrm{true}}\|_2}. \tag{29}$$

This is possible when using synthetic data, since we know the true distribution function. The relative error norm for different regularisation parameters are shown in figure 7 for reconstructions of three different true distributions. For the blue data points with a minimum relative error of $\varepsilon \sim 0.8$ only first-order Tikhonov regularisation has been used in the inverse problem. For the red data points with a minimum relative error of $\varepsilon < 0.7$ both first-order Tikhonov regularisation and ICRF regularisation has been used. The better performance in this case is due to the added prior information provided by the ICRF regularisation. The true distributions as well as the optimal reconstructions in each case are shown in figures 8–10.

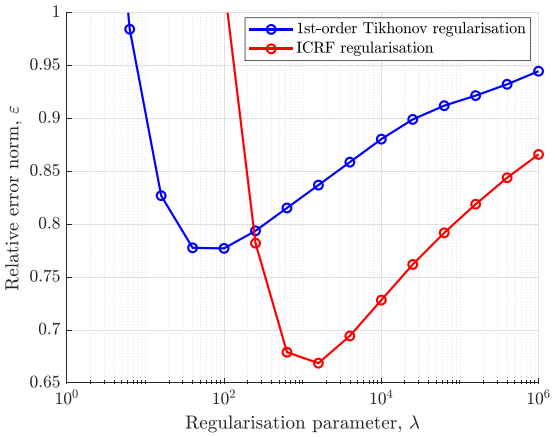

(a) On-axis resonance heating, $R_{\text{birth}} = 7.20$ m

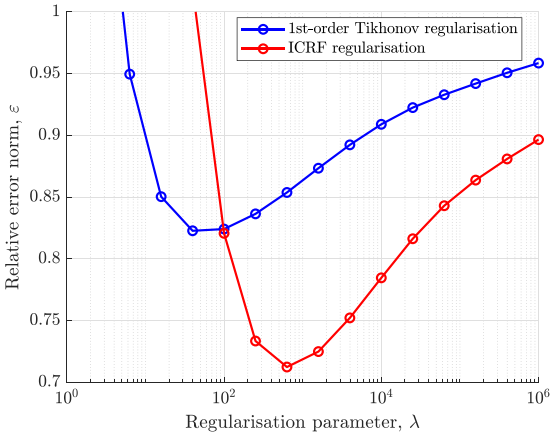

(b) On-axis resonance heating, $R_{\text{birth}} = 7.50$ m

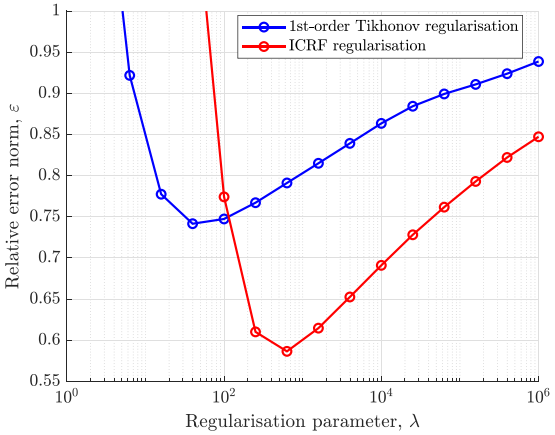

(c) Off-axis resonance heating, $R_{\text{birth}} = 7.20$ m

Figure 7. Relative error norm between the reconstructions and the true distribution for different regularisation parameters. (*a*) On-axis resonance heating with true distribution generated from fast-ion orbits born around $R = 7.20$ m along the NBI beamline. (*b*) On-axis resonance heating with true distribution generated from fast-ion orbits born around $R = 7.50$ m along the NBI beamline. (*c*) Off-axis resonance heating with true distribution generated from fast-ion orbits born around $R = 7.20$ m along the NBI beamline.

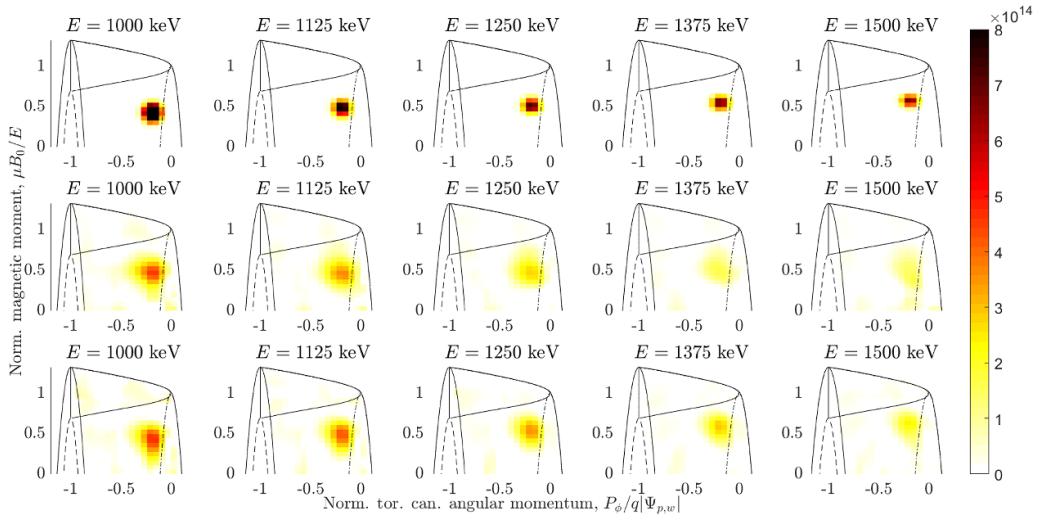

Figure 8. First row: true distribution of ICRF-tail from fast-ion orbits born around $R = 7.20$ m along the NBI beamline with on-axis resonance heating. Second row: optimal reconstruction using only first-order Tikhonov regularisation. Third row: optimal reconstruction using both first-order Tikhonov regularisation and ICRF regularisation.

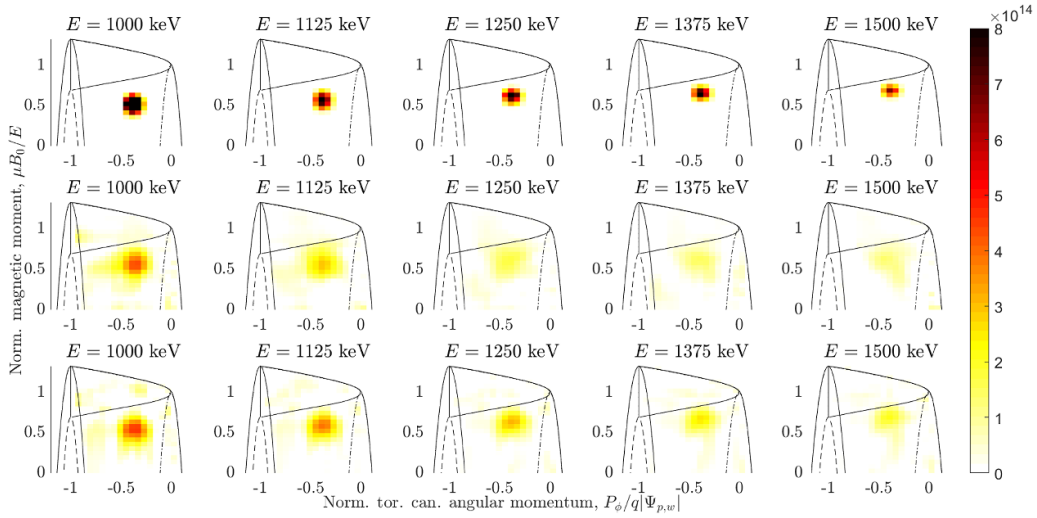

Figure 9. As figure 8 but for fast ions born around $R = 7.50$ m.

First-order Tikhonov regularisation alone does a good job in reconstructing the true distribution in both cases, but, especially for higher energies, it smooths out the distribution too heavily and fails to clearly identify the peak of the distribution. Both these issues are less pronounced when including ICRF regularisation. The ability to better identify the peak of the distribution can be attributed to the ICRF streamlines as shown in figure 1. As noted previously, the streamlines primarily go in the energy direction, to a lesser extent in Λ-direction and have a negligible component in the P_ϕ-direction. This enables the regularisation to drag the peak in the $E = 1000$ keV energy plane up into higher energies. The same reasoning can explain how the ICRF regularisation can improve the localisation of the distribution in each energy plane. The reconstruction is allowed to have larger gradients in the P_ϕ and Λ directions compared to the energy direction, according to the direction of the streamlines.

We finish this section with a comment on how to choose the regularisation parameter in cases where the true distribution is not known, as is the case when inverting experimental data. The choice of the regularisation parameter from experimental data is an important and challenging topic, and many methods have been proposed, see the overview in chapter 5 of [85]. In general, it is not possible to favour one parameter-selection method over the others, since the behaviour of the methods are very problem dependent. The recommendation is to choose the best method from computer simulations, combined with machine learning [86] and visual inspection of the results.

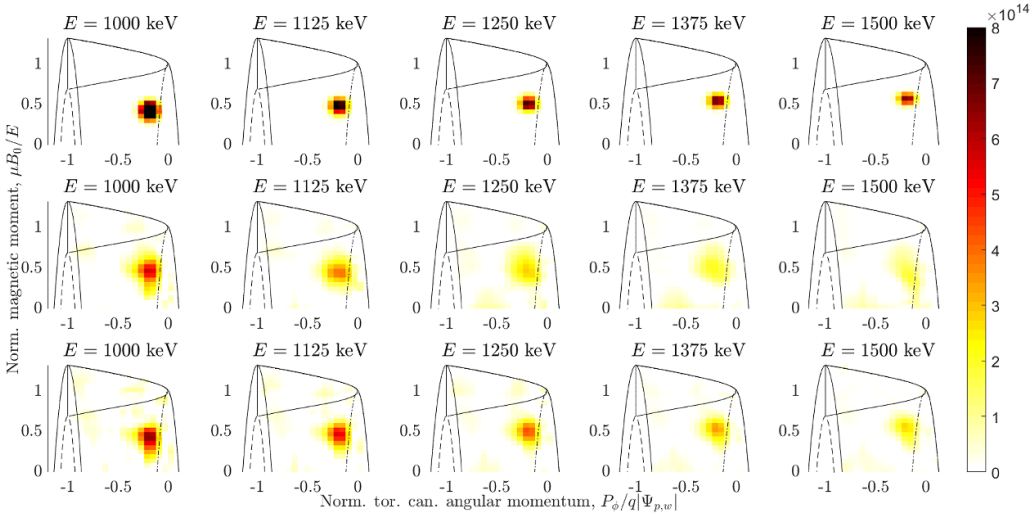

Figure 10. As figure 8, but for off-axis resonance heating and fast ions born around $R = 7.20$ m.

4. Conclusion and outlook

In this paper, we considered wave frequencies on the order of the cyclotron frequency to include wave–particle interactions as prior information in the inverse problem of reconstructing the fast-ion distribution function in tokamak plasmas. The streamlines in constants-of-motion phase space given by the relative change of energy, toroidal canonical angular momentum and normalised magnetic moment have been reviewed and applied in the construction of a regularisation matrix that penalises large gradients along the streamlines. The resonance condition is employed to only regularise according to ICRF physics in those regions of phase space that can satisfy the resonance condition. It is demonstrated that the inclusion of ICRF physics as prior information improves the reconstruction of a test distribution based on synthetic signals using an ITER equilibrium. This prior information can be beneficial for ITER and other future tokamaks with a limited phase-space coverage by the fast-ion diagnostics. It is noted that in case of low-frequency waves the change in normalised magnetic moment is replaced by the conservation of magnetic moment, and the present formalism can therefore be adapted for such a case in a straightforward manner. This would allow the possibility of incorporating information about the interaction between fast-ions and modes such as neoclassical tearing modes and Alfvén eigenmodes in the inverse problem.

Acknowledgments

This work was supported by the Villum Synergy Grant No. VIL50096 from the Villum Foundation.

This work has been carried out within the framework of the EUROfusion Consortium, funded by the European Union via the Euratom Research and Training Programme (Grant Agreement No. 101052200 — EUROfusion). Views and opinions expressed are however those of the author(s) only and do not necessarily reflect those of the European Union or the European Commission. Neither the European Union nor the European Commission can be held responsible for them.

ORCID iDs

M. Rud https://orcid.org/0000-0003-2482-4461
J. Eriksson https://orcid.org/0000-0002-0892-3358
P.C. Hansen https://orcid.org/0000-0002-7333-7216
H. Järleblad https://orcid.org/0000-0003-1126-686X
Ye.O. Kazakov https://orcid.org/0000-0001-6316-5441
S.B. Korsholm https://orcid.org/0000-0001-7160-8361
M. Nocente https://orcid.org/0000-0003-0170-5275
J. Rasmussen https://orcid.org/0000-0002-3947-1518
B.C.G. Reman https://orcid.org/0000-0003-3507-9444
A. Valentini https://orcid.org/0009-0003-5394-4267
Y. Dong https://orcid.org/0000-0001-8363-9448
D. Moseev https://orcid.org/0000-0001-7955-8565
M. Salewski https://orcid.org/0000-0002-3699-679X

References

[1] Mazzi S. *et al* (JET Contributors) 2022 *Nature* **18** 776–82
[2] Heidbrink W.W. 2008 *Phys. Plasma* **15** 055501
[3] Heidbrink W.W. and White R.B. 2020 *Phys. Plasma* **27** 030901
[4] Gorelenkov N.N., Pinches S.D. and Toi K. 2014 *Nucl. Fusion* **54** 125001
[5] Mc Clements K.G. and Fredrickson E.D. 2017 *Plasma Phys. Control. Fusion* **59** 053001
[6] Pinches S.D., Chapman I.T., Lauber P.W., Oliver H.J.C., Sharapov S.E., Shinohara K. and Tani K. 2015 *Phys. Plasma* **22** 021807
[7] Todo Y. 2019 *Rev. Mod. Plasma Phys.* **3** 1
[8] Hastie R.J. 1997 *Astrophys. Space Sci.* **256** 177–204
[9] Garcia-Munoz M. *et al* (the ASDEX Upgrade Team) 2011 *Nucl. Fusion* **51** 103013
[10] Nabais F., Borba D., Garcia-Muñoz M., Johnson T., Kiptily V.G., Reich M., Nave M.F.F., Pinches S.D. and Sharapov S.E. (JET-EFDA contributors) 2010 *Nucl. Fusion* **50** 115006

[11] Heidbrink W.W. *et al* 2014 *Plasma Phys. Control. Fusion* **56** 095030
[12] Fredrickson E.D. *et al* 2009 *Phys. Plasma* **16** 122505
[13] Podestà M. *et al* 2009 *Phys. Plasma* **16** 056104
[14] Hadamard J. 1902 *Princeton University Bulletin* **13** 49–52
[15] Salewski M. *et al* (the ASDEX Upgrade Team) 2012 *Nucl. Fusion* **52** 103008
[16] Salewski M. *et al* (the ASDEX Upgrade Team) 2013 *Nucl. Fusion* **53** 063019
[17] Salewski M. *et al* (the ASDEX Upgrade Team) 2014 *Nucl. Fusion* **54** 023005
[18] Weiland M., Geiger B., Jacobsen A. S., Reich M., Salewski M. and Odstrčil T. (the ASDEX Upgrade Team) 2016 *Plasma Phys. Control. Fusion* **58** 025012
[19] Jacobsen A.S. *et al* 2016 *Plasma Phys. Control. Fusion* **58** 042002
[20] Geiger B. *et al* (the TCV Team and the EUROfusion MST1 Team) 2017 *Plasma Phys. Control. Fusion* **59** 115002
[21] Madsen B. *et al* 2018 *Rev. Sci. Instrum.* **89** 10D125
[22] Madsen B., Salewski M., Heidbrink W.W., Stagner L., Podestà M., Lin D., Garcia A.V., Hansen P.C. and Huang J. (the DIII-D Team) 2020 *Nucl. Fusion* **60** 066024
[23] Madsen B. *et al* 2020 *Plasma Phys. Control. Fusion* **62** 115019
[24] Järleblad H. *et al* 2025 *Nucl. Fusion* **65** 016060
[25] Salewski M. *et al* (JET Contributors) 2017 *Nucl. Fusion* **57** 056001
[26] Weiland M., Bilato R., Geiger B., Schneider P.A., Tardini G., Garcia-Muñoz M., Ryter F., Salewski M. and Zohm H. (the ASDEX Upgrade Team and the EUROfusion MST1 Team) 2017 *Nucl. Fusion* **57** 116058
[27] Reman B.C.G. *et al* Velocity-space tomography of a three-ion scheme ICRF distribution function at jet *Nucl. Fusion* (submitted)
[28] Salewski M. *et al* (the ASDEX Upgrade Team) 2016 *Nucl. Fusion* **56** 106024
[29] Salewski M. *et al* 2018 *Nucl. Fusion* **58** 096019
[30] Schmidt B.S. *et al* (the ASDEX Upgrade Team) 2024 *Nucl. Fusion* **64** 106053
[31] Stagner L., Heidbrink W.W., Salewski M., Jacobsen A.S. and Geiger B. (the DIII-D and ASDEX Upgrade Teams) 2022 *Nucl. Fusion* **62** 026033
[32] Schmidt B.S. *et al* 2023 *Nucl. Fusion* **63** 076016
[33] Rud M. *et al* 2024 *Nucl. Fusion* **64** 076018
[34] Gorelenkov N.N., Cheng C.Z. and Fu G.Y. 1999 *Phys. Plasmas* **6** 2802–7
[35] Podestà M., Gorelenkova M. and White R.B. 2014 *Plasma Phys. Control. Fusion* **56** 055003
[36] Podestà M., Gorelenkova M., Gorelenkov N.N. and White R.B. 2017 *Plasma Phys. Control. Fusion* **59** 095008
[37] Podestà M., M. Gorelenkova, A.A. Teplukhina, P.J. Bonofiglo, R. Dumont, D. Keeling, F.M. Poli and R.B. White (JET Contributors) 2022 *Nucl. Fusion* **62** 126047
[38] Podestà M. *et al* 2021 *Plasma Phys. Control. Fusion* **64** 025002
[39] Todo Y., Van Zeeland M.A., Bierwage A., Heidbrink W.W. and Austin M.E. 2015 *Nucl. Fusion* **55** 073020
[40] Chen L. and Zonca F. 2016 *Rev. Mod. Phys.* **88** 015008
[41] Eriksson L.-G., Mantsinen M.J., Hellsten T. and Carlsson J. 1999 *Phys. Plasmas* **6** 513–8
[42] Kaufman A.N. 1972 *Phys. Fluids* **15** 1063–9
[43] Eriksson L.-G. and Helander P. 1994 *Phys. Plasmas* **1** 308–14
[44] Stix T.H. 1975 *Nucl. Fusion* **15** 737
[45] Korsholm S.B. *et al* 2010 *Nucl. Instrum. Methods Phys. Res.* A **623** 677–80
[46] Korsholm S.B. *et al* 2022 *Rev. Sci. Instrum.* **93** 103539
[47] Rasmussen J., Stejner M., Jensen T., Klinkby E.B., Korsholm S.B., Larsen A.W., Leipold F., Nielsen S.K. and Salewski M. 2019 *Nucl. Fusion* **59** 096051
[48] Rasmussen J., Girard E. and Korsholm S.B. (Private communications) 2022 *Technical report* ITER IDM Ref. ITER D UXVCNQ (Technical University of Denmark)
[49] Salewski M. *et al* 2009 *Plasma Phys. Control. Fusion* **51** 035006
[50] Salewski M., Eriksson L.-G., Bindslev H., Korsholm S.B., Leipold F., Meo F., Michelsen P.K. and Nielsen S.K. 2009 *Nucl. Fusion* **49** 025006
[51] Nocente M. *et al* 2017 *Nucl. Fusion* **57** 076016
[52] Kazakov Y., Van Eester D., Dumont R. and Ongena J. 2015 *Nucl. Fusion* **55** 032001
[53] Kazakov Y.O. *et al* (JET Contributors, ASDEX Upgrade Team, EUROfusion MST1 Team, Alcator C-Mod Team) 2021 *Phys. Plasmas* **28** 020501
[54] Sharapov S.E. *et al* (JET Team) 2000 *Nucl. Fusion* **40** 1363
[55] Bobkov V. *et al* 2021 *Nucl. Fusion* **61** 046039
[56] Eriksson L.-G. *et al* 1998 *Phys. Rev. Lett.* **81** 1231–4
[57] Mantsinen M.J. *et al* 2002 *Phys. Rev. Lett.* **89** 115004
[58] Stagner L. and Heidbrink W.W. 2017 *Phys. Plasma* **24** 092505
[59] Järleblad H. *et al* 2021 *Rev. Sci. Instrum.* **92** 043526
[60] Järleblad H., Stagner L., Salewski M., Eriksson J., Nocente M., Rasmussen J., Štancar Ž., Kazakov Y.O. and Simmendefeldt B. (JET Contributors) 2022 *Nucl. Fusion* **62** 112005
[61] Benjamin S., Järleblad H., Salewski M., Stagner L., Hole M. and Pfefferlé D. 2023 *Comput. Phys. Commun.* **292** 108893
[62] Hellsten T. , Johnson T., Carlsson J., Eriksson L.-G., Hedin J., Laxåback M. and Mantsinen M. 2004 *Nucl. Fusion* **44** 892
[63] Du X.D. *et al* 2021 *Phys. Rev. Lett.* **127** 235002
[64] Imbeaux F. *et al* 2015 *Nucl. Fusion* **55** 123006
[65] Pinches S. *et al* 2018 Progress in the ITER integrated modelling programme and the ITER scenario database *2018 IAEA Fusion Energy Conf.* (*Gandhinagar, 22–27 October 2018*) p 504
[66] White R.B. 2001 *The Theory of Toroidally Confined Plasmas* (Imperial College Press)
[67] Dendy R.O., Hastie R.J., Mc Clements K.G. and Martin T.J. 1995 *Phys. Plasmas* **2** 1623–36
[68] Bilato R., Odstrcil T., Casson F.J., Angioni C., Brambilla M., Kazakov Y.O. and Poli E. 2017 *Nucl. Fusion* **57** 056020
[69] Järleblad H., Stagner L., Salewski M., Eriksson J., Nocente M., Schmidt B.S. and Larsen M. R. 2024 *Comput. Phys. Commun.* **294** 108930
[70] Järleblad H. *et al* (JET Contributors) 2024 *Nucl. Fusion* **64** 026015
[71] Rud M. *et al* 2024 *Nucl. Fusion* **64** 036007
[72] Moseev D. *et al* 2018 *Reviews of Modern Plasma Physics* **2** 7
[73] Heidbrink W.W. *et al* 2007 *Plasma Phys. Control. Fusion* **49** 1457
[74] Heidbrink W.W., K.H. Burrell, Y. Luo, N.A. Pablant and E. Ruskov 2004 *Plasma Phys. Control. Fusion* **46** 1855–75
[75] Heidbrink W.W. 2010 *Rev. Sci. Instrum.* **81** 10D727
[76] Salewski M. *et al* (the ASDEX Upgrade Team) 2014 *Plasma Phys. Control. Fusion* **56** 105005

[77] Salewski M. *et al* 2011 *Nucl. Fusion* **51** 083014
[78] Salewski M. *et al* (JET Contributors) 2015 *Nucl. Fusion* **55** 093029
[79] Salewski M. *et al* (JET Contributors) 2016 *Nucl. Fusion* **56** 046009
[80] Tikhonov A.N. and Arsenin V.Y. 1977 *Solutions of Ill-Posed Problems* (*Scripta Series in Mathematics*) (V. H. Winston & Sons)
[81] Johnson T. and Eriksson L.-G. 2024 *Fundamental Plasma Physics* **11** 100065
[82] Brank M. *et al* 2021 *Nucl. Materials and Energy* **27** 101021
[83] Schneider M. *et al* (JET Contributors) 2016 *Nucl. Fusion* **56** 112022
[84] Petrov Y.V. and Harvey R.W. 2016 *Plasma Phys. Control. Fusion* **58** 115001
[85] Hansen P.C. 2010 *Society for Industrial and Applied Mathematics* (available at: https://epubs.siam.org/doi/abs/10.1137/1.9780898718836)
[86] Afkham B.M., Chung J. and Chung M. 2021 *Inverse Problems* **37** 105017